remote sensing

MDPI

Article

Modeling and Data Analysis of Bistatic Bottom Reverberation from a Towed Horizontal Array

Zhaohua Su [1,2], Jie Zhuo [1,2,*] and Chao Sun [1,2]

[1] School of Marine Science and Technology, Northwestern Polytechnical University, Xi'an 710072, China; suzh@mail.nwpu.edu.cn (Z.S.); csun@nwpu.edu.cn (C.S.)
[2] Shaanxi Key Laboratory of Underwater Information Technology, Xi'an 710072, China
* Correspondence: jzhuo@nwpu.edu.cn

Abstract: The spatial-temporal structures of bottom reverberation are associated with seafloor features. In a bistatic bottom reverberation experiment involving a vertical transmitting array and a towed horizontal receiving array, stable stripe structures were observed within the beam-time domain. In this study, a bistatic reverberation model based on ray theory is presented to interpret the experimental phenomena. The conventional empirical scattering function is primarily applicable to small grazing angles. Moreover, the regional segmentation method simulates reverberations across various receiving beams, ignoring scatterers in other areas. To address these issues, we substitute the empirical scattering function with a small-slope approximation (SSA) that is appropriate for full grazing angles. Furthermore, we utilize the beam pattern of arrays to incorporate the effects of each scatterer, and derive the expression for bottom reverberation intensity in both the array and beam domains. The established model demonstrates its applicability in simulating and interpreting the stripe structures of bottom reverberation, and the comparison shows that the model outputs are in agreement with the experimental results. The analysis indicates that the vertical stripes within the structures originate from eigenrays in the mirror reflection direction. Furthermore, the convex stripes are predominantly affected by the direct ray and the surface reflection ray among the scattered eigenrays, whereas the concave and elliptical stripes are primarily affected by the bottom-surface reflection ray and the surface-bottom-surface reflection ray within the scattered eigenrays.

Keywords: bottom reverberation; spatial-temporal structures; bistatic sonar; model establishment

check for updates

Academic Editors: Xuebo Zhang, Haiyong Xu, Jingyue Lu, Lei Zhang, Marc Pinto and Farman Ali

Received: 20 November 2024
Revised: 6 January 2025
Accepted: 6 January 2025
Published: 8 January 2025

Citation: Su, Z.; Zhuo, J.; Sun, C. Modeling and Data Analysis of Bistatic Bottom Reverberation from a Towed Horizontal Array. *Remote Sens.* **2025**, *17*, 192. https://doi.org/10.3390/rs17020192

Copyright: © 2025 by the authors. Licensee MDPI, Basel, Switzerland. This article is an open access article distributed under the terms and conditions of the Creative Commons Attribution (CC BY) license (https://creativecommons.org/licenses/by/4.0/).

1. Introduction

As a critical boundary for ocean waveguides, the seabed exhibits significant reflection and scattering effects on acoustic waves. Bottom reverberation results from the superposition of scattering echoes generated by numerous seafloor scatterers, encapsulating rich information about the ocean environment [1,2], which is widely utilized in analyzing the seafloor substrate and the inversion of parameters [3,4]. Owing to multipath propagation, each combination of incident and scattered rays contributes to bottom reverberation, resulting in a multi-peak structure [5]. By employing a vertical or horizontal array, the receiving signals can be beamformed to obtain the spatial-temporal structures of a bottom reverberation. The complex spatial-temporal distribution is an important feature that is closely associated with seabed topography [5–7]. Utilizing numerical methods to model bottom reverberation, researchers can analyze the shape characteristics of spatial-temporal struc-

tures. This approach is significant and useful for engineering applications investigating the generation of these structures and their association with seafloor features.

Two approaches are prevalently employed to model reverberation. The first is the full-wave model [8–11], which utilizes the wave equation to depict the propagation and scattering of reverberation, offering a rigorous theoretical expression. The second is a combination of the sound propagation model and the scattering model. In the sound propagation model, bottom reverberation models mainly include normal mode-based models [12–14], ray-based models [15,16], and parabolic equation models [17,18]. This latter approach is more pragmatic and applicable in analyzing the characteristics of measured reverberation.

Previous studies have demonstrated that large-scale topography and coastal slopes give rise to intense bottom reverberation [19–23]. The above approach has been employed to identify unknown features by modeling reverberation and comparing model outputs with data [22,23]. Among these outputs, local peaks in reverberation are associated with bathymetric features, while abnormal peaks align with unknown seafloor features. In the Mid-Atlantic Ridge (MAR) experiment, a range-dependent parabolic equation model was employed to calculate transmission loss (TL). The comparison with the echoes reveals that significant scattered echoes originated from the steep escarpments and cliffs, and are highly correlated with TL [19–21]. Moreover, a bistatic sonar system with a horizontal receiving array and two low-frequency vertical source arrays was employed in the continental shelf area [6]. The obtained beam data were projected onto Cartesian coordinates, revealing that the echoes in the reverberation mainly came from a preset tubular target and an underground channel. Subsequently, the researchers utilized a range-dependent parabolic equation model to rectify the scattering intensity of the inflated target [24,25]. Additionally, Preston and Ellis [22,23] employed ray theory and the Lambert scattering function to model the reverberation received by the towed array. They superimposed a polar map of the reverberation onto a topographic map, identifying unknown features and extracting seabed information through model–data comparisons. Furthermore, an adiabatic normal mode-based model was employed to analyze and handle seafloor scattering and clutter echoes in the Target and Reverberation Experiment 2013 (TREX13) [26,27]. In addition, researchers have employed the scattering model and the statistical model to investigate the causes and statistical characteristics of strong scattering in seafloor reverberation on the Malta Plateau [28–31]. Furthermore, in an experiment conducted on the Ulleung Basin [32,33], a depth-bistatic bottom reverberation model was developed to predict reverberation from an active triple-towed array, and the influence of continental shelf topography on the drop-off regions in the bearing-time records was analyzed.

In the aforementioned studies, the Lambert scattering function was typically employed to compute the scattering intensity of the interface [15,34]. This empirical function mainly applies to small grazing angles, and its coefficients have no quantitative correlation with seabed parameters. Seabed areas are divided by azimuth angles to simulate reverberation at different receiving angles, ignoring scatterers in other regions [35]. Additionally, the scattering region that contributes to reverberation at a specific time is regarded as an elliptic ring in the conventional method. This approach disregards the disparity in the propagation time of eigenrays at each seafloor scatterer. Owing to multipath structures, scatterers that impact reverberation do not lie exactly on the same ellipse.

In a bistatic bottom reverberation experiment conducted in the northern South China Sea in August 2020, with a vertical transmitting array and a towed horizontal array, the stable spatial-temporal structures of bottom reverberation were observed at different receiving positions. These structures are related to the paths of the incident and scattered rays, presenting vertical, curved, and elliptical stripes in the beam-time domain.

This study presents a bistatic bottom reverberation model based on ray theory. These stripes are modeled, and the experimental phenomena are analyzed and interpreted. Instead of the empirical scattering function, the small-slope approximation (SSA) [36,37] is adopted for full grazing angles. The seabed is sectioned into rectangular grids to obtain accurate propagation delays, and the beam patterns of the transmitting array and the receiving array are utilized to account for each grid's influence on reverberation. The established model enables the calculation of reverberation intensity within the element or beam domain, and simulate the spatial-temporal structures of reverberation from the horizontal array. The model outputs reproduce the stripe structures observed in the experiment, interpreting the generation of the structures by specifying the types of incident and scattered rays.

This paper is organized as follows: Section 2 establishes a bistatic bottom reverberation model with a vertical transmitting array and a horizontal receiving array. Section 3 presents an overview of the experiment. Section 4 compares the model results and the experimental results, and explains the experimental phenomena. Finally, Section 5 summarizes the conclusions.

2. Bistatic Bottom Reverberation Model

2.1. Bistatic Bottom Reverberation Scene and the Parameters

The bistatic system consists of a vertical transmitting array and a towed horizontal receiving array; the bottom reverberation scene is depicted in Figure 1. Each transmission is referred to as a single ping. During each transmission, the sound waves emitted by the source are scattered on the seafloor and then propagated to the receiver, resulting in bottom reverberation. Typically, sound propagation models are combined with scattering models to simulate reverberation. In this section, the ray model is employed to describe underwater acoustic propagation, and the small-slope approximation (SSA) model is utilized to address the scattering process of the eigenrays with different grazing angles. The influence of multipath propagation is considered in this approach, with the scattered signals along various paths from scatterers contributing to the reverberation signal.

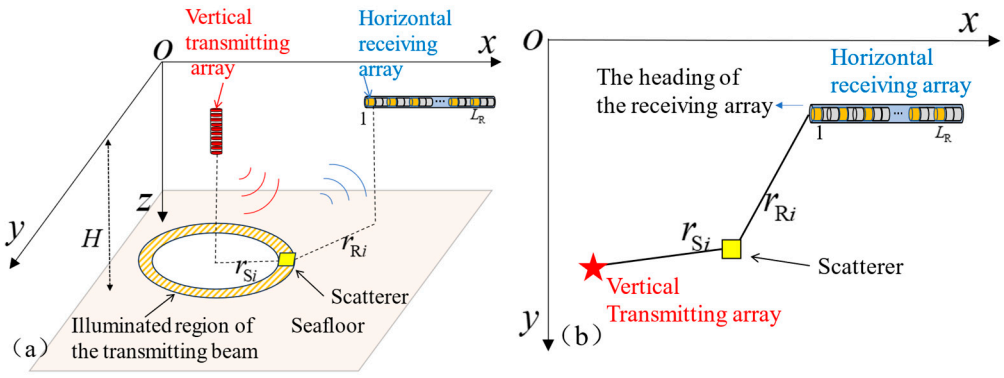


Figure 1. The scene of the bistatic bottom reverberation. (**a**) Bistatic sonar geometry and an element scattering area. (**b**) Top view of the scene.

The water depth in a horizontally layered environment is denoted as H, and the sound speed is c. Assume that the source is a vertical linear array of L_S elements with an element spacing of d_S. The center coordinate of the source is denoted as (x_s, y_s, z_S). A horizontal linear array is the receiving array, consisting of L_R elements with an element spacing of d_R. The first receiving element is the reference element, with the coordinate denoted as (x_R, y_R, z_R). Additionally, the coordinate of the unit scatterer is denoted as (x_i, y_i, z_i), and the horizontal distances to the source and the reference element of the receiving array are r_{Si}

and r_{Ri}, respectively. The heading angle of the receiving array is denoted as γ. In this study, γ is defined as 0° in the positive direction of the x-axis, with the counterclockwise direction corresponding to positive angles. To derive and present the equations in Section 2.2, we introduce the following vectors: $\mathbf{r}_{Si} = (x_i - x_S, y_i - y_S)$, $\mathbf{r}_{Ri} = (x_R - x_i, y_R - y_i)$, and $\mathbf{r}_\gamma = (\cos\gamma, \sin\gamma)$.

Figure 2a,b illustrates the schematic diagrams of the transmitting beam angle and the receiving beam angle, respectively. For the vertical linear array in Figure 2a, the beam pattern is symmetrical around the axis of the array within the xy-plane. In the vertical dimension, the transmitting beam angle is designated as θ_S, and the clockwise direction corresponds to the positive angle of the transmitting beam. Specifically, θ_S is denoted as −90° when the beam angle is toward the sea surface, and 90° when the beam angle is toward the seafloor. For the horizontal linear array in Figure 2b, the beam pattern exhibits symmetry around the axis of the array within the z plane, and the receiving beam angle is denoted as θ_R. θ_R is equal to −90° when the beam is directed toward the head of the receiving array, and 90° when the beam points at the tail of the array.

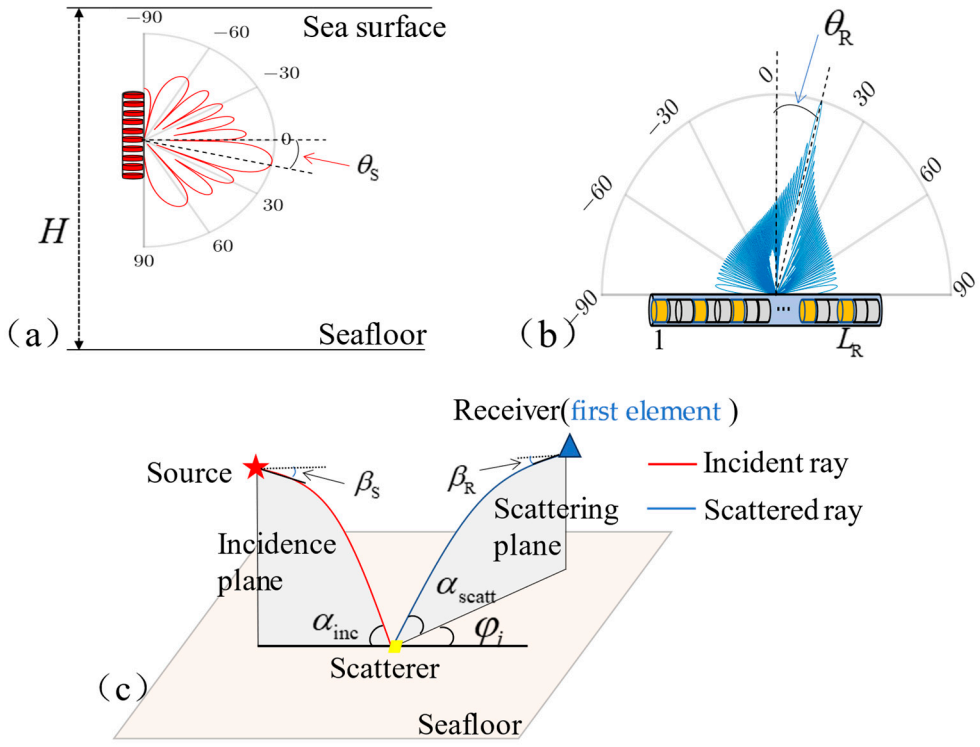


Figure 2. Angle parameters involved in the model. (**a**) The transmitting beam angle θ_S. (**b**) The receiving beam angle θ_R. (**c**) The exit grazing angle β_S of the incident ray, the arrival grazing angle β_R of the scatter, the incident grazing angle α_{inc}, the scattered grazing angle α_{scatt}, and the scattered azimuth angle φ_i at the seafloor scatterer.

The incident plane and the scattering plane are typically non-coplanar, as illustrated in Figure 2c. The variables β_S and β_R represent the exit grazing angle of the incident ray at the source and the arrival grazing angle of the scattered ray at the first receiving element, respectively. In the three-dimensional scattering function $g(\alpha_{inc}, \alpha_{scatt}, \varphi_i)$ of the seafloor interface, the variables α_{inc}, α_{scatt}, and φ_i represent the incident grazing angle, the scattered grazing angle, and the scattered azimuth angle, respectively. In addition, the incidence plane and the scattering plane are coplanar within the vertical plane when $\varphi_i = 0°$, which is referred to as the mirror reflection direction.

2.2. Theoretical Derivation of Expressions for Bistatic Bottom Reverberation Model

According to ray theory, we can suppose that the coordinate of the point source is (x_S, y_S, z_S); thus, the sound pressure at the unit scatterer with the coordinate (x_i, y_i, z_i) can be expressed as

$$\begin{cases} p(x_i, y_i, z_i) = \sum_{m=1}^{M} A_{\mathrm{inc},m} e^{j\omega\tau_{\mathrm{inc},m}} \\ A_{\mathrm{inc},m} = \sqrt{\dfrac{W\cos\beta_{Sm}}{r_{Si}\left|\partial r_{Si}/\partial\beta\right|_{\beta_{Sm}}\sin\alpha_{\mathrm{inc},m}}} \\ \tau_{\mathrm{inc},m} = \left(r_{Si}\cos\beta_{Sm} + \int_{z_S}^{H}\sqrt{\eta^2(z)-\cos^2\beta_{Sm}}dz\right)/c \end{cases} \tag{1}$$

where M is the number of incident eigenrays, and $A_{\mathrm{inc},m}$ and $\tau_{\mathrm{inc},m}$ are the amplitude and propagation delay of the mth incident eigenray, respectively. $\omega = 2\pi f$ is the angular frequency and f is the frequency of the source. W represents the radiated power per unit solid angle, and $r_{Si} = |\mathbf{r}_{Si}|$ represents the horizontal distance between the source and the seafloor scatterer. β_{Sm} and $\alpha_{\mathrm{inc},m}$ are the exit grazing angle of the mth incident eigenray at the source and the incident grazing angle at the seafloor, respectively. In addition, $\eta(z) = c(z)/c(z_S)$ is the refractive rate.

For the vertical transmitting array, the transmitting signal of each element can be weighted through beamforming methods. Consequently, the sound pressure in Equation (1) can be represented as

$$p(x_i, y_i, z_i) = \sum_{m=1}^{M} A_{\mathrm{inc},m} B_S(\beta_{Sm};\theta_S) e^{j\omega\tau_{\mathrm{inc},m}} \tag{2}$$

where $B_S(\beta_{Sm};\theta_S)$ is the beam pattern of the transmitting array, and θ_S represents the polar angle of the transmitting beam.

According to the reciprocity theorem, the sound pressure received by the reference element of the receiving array can be expressed as follows (the coordinates (x_i, y_i, z_i) are omitted)

$$p_1 = \sum_{m=1}^{M}\sum_{n=1}^{N} A_{\mathrm{inc},m} A_{\mathrm{scatt},n} B_S(\beta_{Sm};\theta_S) g(\alpha_{\mathrm{inc},m}, \alpha_{\mathrm{scatt},n}, \varphi_i) e^{j\omega(\tau_{\mathrm{inc},m}+\tau_{\mathrm{scatt},n})} \tag{3}$$

where N is the number of the scattered eigenrays, and $A_{\mathrm{scatt},n}$ and $\tau_{\mathrm{scatt},n}$ are the amplitude and propagation delay of the nth scattered eigenray, respectively. The amplitudes and delays of both the incident and scattered eigenrays are computed utilizing the Bellhop model [38].

The three-dimensional scattering model in the literature [37] is expressed as

$$\begin{aligned} G(\alpha_{\mathrm{inc},m}, \alpha_{\mathrm{scatt},n}, \varphi_i) &= \left|\mathrm{g}(\alpha_{\mathrm{inc},m}, \alpha_{\mathrm{scatt},n}, \varphi_i)\right|^2 \\ &= \frac{k_{ww}^2 |R_{ww}(\alpha_{\mathrm{inc},m}, \alpha_{\mathrm{scatt},n}, \varphi_i)|^2}{2\pi(\Delta Q)^2(\Delta Q_z)^2} \cdot \int_0^{+\infty} J_0(u) u e^{-qu^{2v}} du \end{aligned} \tag{4}$$

where

$$\Delta Q = k_{ww}\sqrt{\cos^2\alpha_{\mathrm{inc},m} + \cos^2\alpha_{\mathrm{scatt},n} - 2\cos\alpha_{\mathrm{inc},m}\cos\alpha_{\mathrm{scatt},n}\cos\varphi_i} \tag{5}$$

$$\Delta Q_z = k_{ww}(\sin\alpha_{\mathrm{inc},m} + \sin\alpha_{\mathrm{scatt},n}) \tag{6}$$

$$q = \frac{\pi w_2 (\Delta Q_z)^2}{(2\cdot\Delta Q)^{2v}} \cdot \frac{\Gamma(2-v)}{v(1-v)\Gamma(1+v)} \tag{7}$$

$$v = \frac{\gamma_2}{2} - 1 \tag{8}$$

where k_{ww} is the wavenumber, ΔQ represents the magnitude of the difference between the horizontal components of the incident wave vector and that of the scattered wave vector, and ΔQ_z corresponds to the difference between the vertical components of these two vectors. In the "Kirchhoff integral" to the right of Equation (4), J_0 is the 0-order Bessel function of the first kind, and Γ is the gamma function. w_2 and γ_2 are the spectral strength and spectral exponent for the rough interface, respectively. The expression of variable $R_{ww}(\alpha_{\mathrm{inc},m}, \alpha_{\mathrm{scatt},n}, \varphi_i)$ varies depending on the type of seafloor utilized, and the specific representation employed in this study is detailed in Appendix A.

By employing the far-field assumption, the horizontal range from the bottom scatterer to the lth element of the receiving array can be approximately expressed as

$$\begin{cases} r_{\mathrm{R}i,l} \approx r_{\mathrm{R}i} + (l-1)d_{\mathrm{R}} \sin\theta_i, & l = 1, \ldots, L_{\mathrm{R}} \\ \theta_i = \langle \mathbf{r}_\gamma, -\mathbf{r}_{\mathrm{R}i} \rangle - 90^\circ \end{cases} \tag{9}$$

where $\langle \cdot \rangle$ denotes the calculation of the angle between two vectors.

Consequently, the propagation delay of the nth scattered eigenray to the lth element is expressed as

$$\tau_{\mathrm{scatt},n}(l) = \tau_{\mathrm{scatt},n} + (l-1)d_{\mathrm{R}} \sin\theta_i \cos\beta_{Rn}/c_0 \tag{10}$$

where c_0 is the sound speed at the receiver. The variable $\theta'_{i,n}$ is defined as $\sin\theta'_{i,n} = \sin\theta_i \cos\beta_{Rn}$, representing the arrival angle of the nth scattered eigenray at the receiving array.

Combined with Equations (3) and (9), the sound pressure of the lth element can be expressed as

$$p_l = \sum_{m=1}^{M}\sum_{n=1}^{N} A_{\mathrm{inc},m} A_{\mathrm{scatt},n} B_{\mathrm{S}}(\beta_{\mathrm{S}m}; \theta_{\mathrm{S}}) g(\alpha_{\mathrm{inc},m}, \alpha_{\mathrm{scatt},n}, \varphi_i) e^{j\omega(\tau_{\mathrm{inc},m}+\tau_{\mathrm{scatt},n})} e^{j\omega(l-1)d_{\mathrm{R}}\sin\theta'_{i,n}/c_0} \tag{11}$$

Accordingly, the incoherent reverberation intensity of the element is expressed as

$$I_{l,i} = \sum_{m=1}^{M}\sum_{n=1}^{N} |A_{\mathrm{inc},m}|^2 |A_{\mathrm{scatt},n}|^2 |B_{\mathrm{S}}(\beta_{\mathrm{S}m}; \theta_{\mathrm{S}})|^2 |G(\alpha_{\mathrm{inc},m}, \alpha_{\mathrm{scatt},n}, \varphi_i)| \tag{12}$$

At a specific time t, the reverberation of the lth element is represented as the superposition of scattered signals from different scatterers. Then, the reverberation intensity is expressed as

$$RL_l(t) = I_0 \cdot \sum_{i=1}^{K} I_{l,i} \Delta S_i \tag{13}$$

where I_0 is the intensity of the source, t is denoted as $t = \tau_{\mathrm{inc},m} + \tau_{\mathrm{scatt},n}$, K is the number of scatterers contributing to the reverberation, and ΔS_i is the area of the ith scatterer.

The sound pressure of each element in Equation (11) is weighted using the beamforming method. When the angle of the receiving beam is denoted as θ_{R}, the beam output is represented as

$$\begin{aligned} p_{\mathrm{beam}}(\theta_{\mathrm{R}}) &= \sum_{l=1}^{L_{\mathrm{R}}} w_l{}^* p_l \\ &= \sum_{m=1}^{M}\sum_{n=1}^{N} A_{\mathrm{inc},m} A_{\mathrm{scatt},n} B_{\mathrm{S}}(\beta_{\mathrm{S}m}; \theta_{\mathrm{S}}) B_{\mathrm{R}}\left(\theta'_{i,n}; \theta_{\mathrm{R}}\right) g(\alpha_{\mathrm{inc},m}, \alpha_{\mathrm{scatt},n}, \varphi_i) e^{j\omega(\tau_{\mathrm{inc},m}+\tau_{\mathrm{scatt},n})} \end{aligned} \tag{14}$$

where the superscript * denotes the conjugation, w_l is the weighted value of the lth element, and $B_{\mathrm{R}}\left(\theta'_{i,n}; \theta_{\mathrm{R}}\right)$ is the beam pattern of the receiving array.

Consequently, the corresponding incoherent reverberation intensity can be expressed as

$$I_{\text{beam},i}(\theta_{\text{R}}) = \sum_{m=1}^{M}\sum_{n=1}^{N} |A_{\text{inc},m}|^2 |A_{\text{scatt},n}|^2 |B_{\text{S}}(\beta_{\text{S}m};\theta_{\text{S}})|^2 \left|B_{\text{R}}\left(\theta'_{i,n};\theta_{\text{R}}\right)\right|^2 |G(\alpha_{\text{inc},m},\alpha_{\text{scatt},n},\varphi_i)| \quad (15)$$

Similar to Equation (13), the reverberation intensity of the beam angle θ_{R} is expressed as

$$RL_{\text{beam}}(\theta_{\text{R}},t) = I_0 \cdot \sum_{i=1}^{K} I_{\text{beam},i}(\theta_{\text{R}})\Delta S_i \quad (16)$$

where the definitions of parameters I_0, t, K, and ΔS_i are consistent with those in Equation (13).

The theoretical derivation indicates that there is a phase difference in the signal waveform of each element, while the incoherent reverberation intensity of each element is consistent in the array domain. In the beam domain, the signal from each scatterer is modulated by the beam pattern of the receiving array. As a result, the incoherent reverberation intensity within the beam varies with the angle. In summary, Figure 3 presents a flow chart illustrating the calculation of bistatic bottom reverberation in both the array and beam domains.

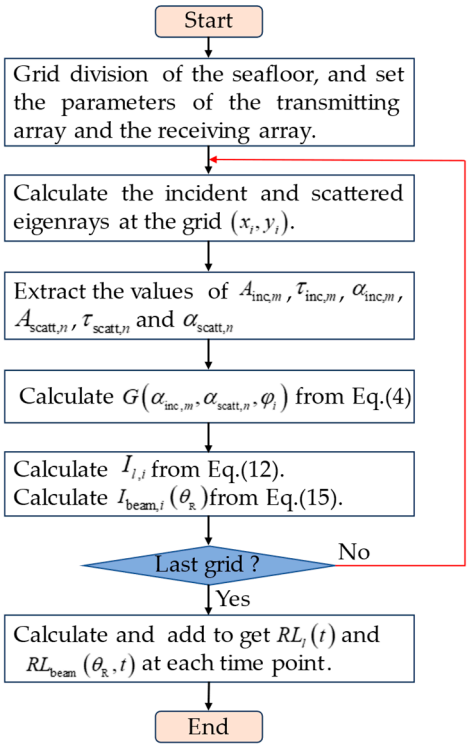


Figure 3. Flow chart for calculating the bistatic bottom reverberation.

3. Overview of Sea Trial Experiment Conducted in the South China Sea

3.1. Experiment Description

In August 2020, an experiment was conducted in the northern South China Sea. The topography of the experimental area, the source site, and the tracks of the receiver are shown in Figure 4a, where "☆" indicates the position of the source and "↑" represents the heading direction of the receiving array. The water depth of the area is approximately 1100 m, with islands and reefs situated to the northwest. In addition, the coordinates of the source are 111.56°E, 16.88°N.

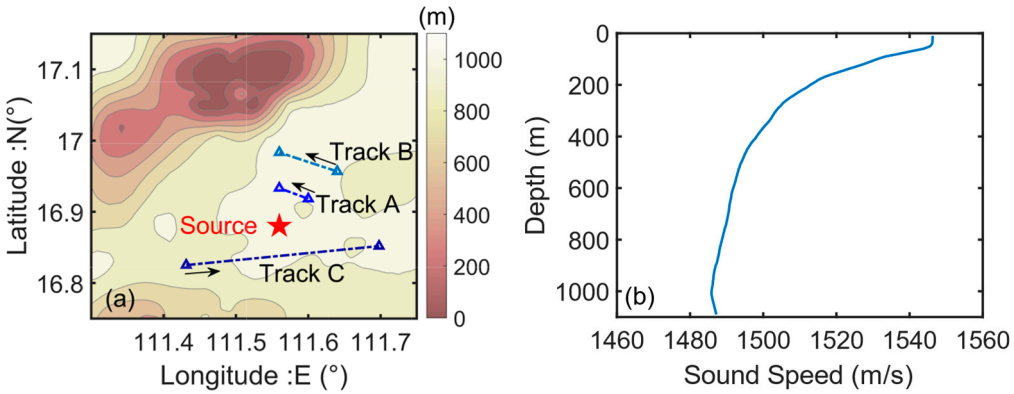


Figure 4. Experimental environment. (**a**) Bathymetry of the area, with depth data obtained from the ETOPO1. (**b**) The sound speed profile measured in the experiment.

The sound speed profile obtained from the experiment is depicted in Figure 4b, exhibiting a typical negative gradient. The sound speed was constant at approximately 1544 m/s within a depth range of 0 to 50 m, and it decreased to about 1484 m/s at the seabed.

The transmitting and receiving arrays utilized in the experiment are shown in Figure 5. The specific parameters are as follows: the source was a 10-element vertical linear array, with an element spacing of 0.42 m, and the receiver was a 96-element towed horizontal linear array, with an element spacing of 0.416 m. Furthermore, the transmitted signal was a linear frequency modulation (LFM) with a frequency ranging from 1700 Hz to 1900 Hz. The duration of each transmission was 1 s, with an interval of 50 s. The source level for each element in the transmitting array was 190 dB, and the sensitivity level of the receiving hydrophone was −142 dB. Additionally, the signal sampling frequency was set 16 kHz.

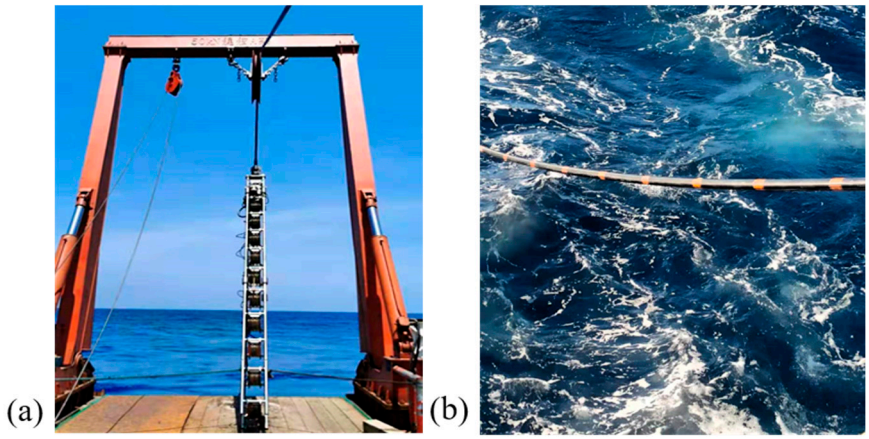


Figure 5. The equipment used in the experiment. (**a**) The transmitting array. (**b**) The receiving array.

During the experiment, the position of the transmitting array was fixed, with a central depth of approximately 52 m. Moreover, the conventional beamforming method was employed to adjust the transmitting beam angle in each transmission. The transmitting beam angle was set to either 0°or 12° in different received tracks. Specifically, the receiving vessel traveled twice along Track A with these transmitting beam angles. Subsequently, the receiving vessel moved along Tracks B and C once each, with transmitting beam angles of 12° for Track B and 0° for Track C.

3.2. Experimental Data Processing

In this section, the data processing is briefly described to obtain the reverberation intensities of the array and beam domains. The received signal of the lth element of the receiving array is denoted as $p'_l(t)$. After being processed through matched filtering, the Fourier transform is applied to derive the spectrum $pp'_l(f)$. At a specific time t, the signal power of the lth element at the center frequency $f_0 = 1800$ Hz is expressed as

$$p'_l(f_0) = \frac{1}{J' f_s (nf_2 - nf_1 + 1)} \sum_{j'=nf_1}^{nf_2} \left| pp'_l(j') \right|^2 \tag{17}$$

where J' represents the number of data sampling points within the period centered on time t, and f_s is the sampling frequency. The variables nf_1 and nf_2 denote the number of frequency points corresponding to the lower and upper bounds of the signal frequency, respectively.

In logarithmic form (unit: dB), the reverberation intensity of the element is as follows

$$RL'_l(t) = 10 \log_{10}\left[p'_l(f_0)\right] - SL - DI - M_v - E_c \tag{18}$$

where SL denotes the source level of a single emitter, and DI represents the directivity index of the transmitting array. M_v is the sensitivity level of the receiving hydrophone and E_c is the processing gain of the matched filter.

Assume that the receiving beam angle is denoted as θ_{rec}. The received signal is processed through conventional beamforming and matching filtering to obtain the beam output, denoted as $p'_{\text{beam}}(\theta_{\text{rec}}, t)$, and the variable $pp_{\text{beam}}(\theta_{\text{rec}}, f)$ represents the spectrum of $p'_{\text{beam}}(\theta_{\text{rec}}, t)$. The average power of the beam output at the center frequency $f_0 = 1800$ Hz is expressed as

$$p'_{\text{beam}}(\theta_{\text{rec}}, f_0) = \frac{1}{J' f_s (nf_2 - nf_1 + 1)} \sum_{j'=nf_1}^{nf_2} \left| pp_{\text{beam}}(\theta_{\text{rec}}, j') \right|^2 \tag{19}$$

where the definitions of the variables J', f_s, nf_1, and nf_2 in Equation (19) are consistent with those in Equation (17).

Similarly, the variable $p'_l(f_0)$ in Equation (18) is substituted with the variable $p'_{\text{beam}}(\theta_{\text{rec}}, f_0)$. Accordingly, the expression of reverberation intensity at the receiving beam angle θ_{rec} is expressed as

$$RL'_{\text{beam}}(\theta_{\text{rec}}, t) = 10 \log_{10}\left[p'_{\text{beam}}(\theta_{\text{rec}}, f_0)\right] - SL - DI - M_v - E_c \tag{20}$$

where the definitions of the variables SL, DI, M_v, and E_c accord with those in Equation (18).

4. Comparison and Interpretation of Simulation and Experimental Results

Following the processing steps in Section 3, the reverberation intensities at a source level of 0 dB in both the array and beam domains are obtained. The results for the experimental data and a comparison between the model and experimental results are presented in this section.

4.1. Parameters of the Simulation Environment

Figure 6 illustrates the simulation environment and the parameters. A single-layer seafloor model was employed, with a seafloor depth of 1100 m. In simulations, we take into account the bathymetry of the experimental area. An $N \times 2D$ ray model is utilized to calculate incident and scattered eigenrays on the seabed grids at different distances,

with the calculations centered on the positions of the source and reference element of the receiving array.

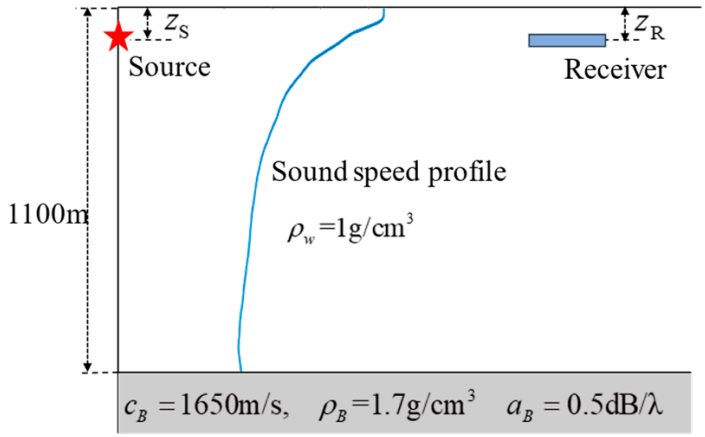


Figure 6. The parameters of the simulation environment.

As the seafloor substrate was not collected during the experiment, a seafloor with sandy substrate was employed and the parameters were appropriately modified. The parameters of the bottom are detailed in Table 1, where a_ρ and a_{wp} represent the ratios of the density and sound speed at the bottom to those in the water, respectively. The variable a_B denotes the attenuation expressed in decibels per wavelength. In addition, w_2 and γ_2 are the spectral strength and spectral exponent for the rough interface, respectively.

Table 1. The parameters of the bottom, where a_ρ, a_{wp}, and γ_2 are dimensionless values.

$a_\rho = \rho_B/\rho_w$	$a_{wp} = c_B/c_w$	a_B (dB/λ)	w_2 ($m^{4-\gamma_2}$)	γ_2
1.7	1.1	0.5	0.006957	3.3

The sound speed profile obtained from measurements is utilized in the simulation. Furthermore, the parameters of the source and the receiving array used in the simulation are consistent with the equipment parameters in the experiment, and the frequency of the sound source is set at 1800 Hz.

4.2. Comparison of Simulation and Experimental Results

This section compares the model output and the experimental results. Regarding the source position as the origin, the latitude and longitude coordinates in Figure 4a were converted into Cartesian coordinates, as depicted in Figure 7. Here, the positive directions of the x-axis and y-axis correspond to the east and north, respectively. We selected experimental data from eight receiving positions, with one signal transmission conducted at each position. The receiving signals at each of these positions were processed according to the procedure described in Section 3.2. The specific parameters are presented in Table 2, including the transmitting beam angle θ_S, the receiving range r_{SR}, depth z_R, the heading angle γ, and the azimuth angle ϕ of the receiver relative to the source in the xoy-plane. Additionally, ϕ is defined as 0° in the positive direction of the x-axis, with the counterclockwise direction corresponding to the positive angles.

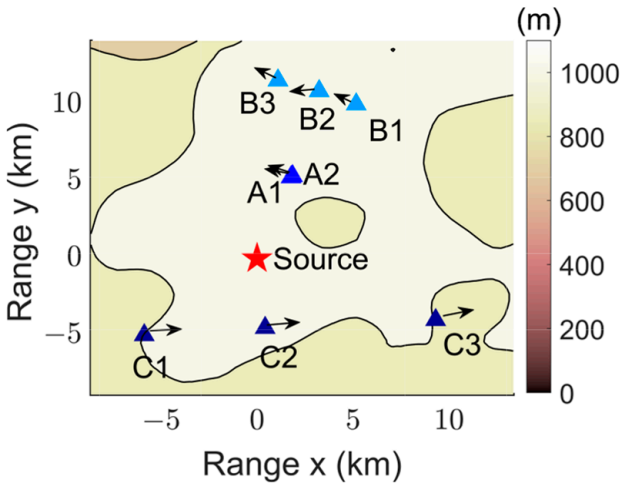


Figure 7. The receiving positions selected for the tracks.

Table 2. Parameter details at different receiving positions.

Position	Transmitting Beam Angle θ_S (°)	Receiving Range r_{SR} (km)	Depth of the Receiver z_R (m)	γ (°)	ϕ (°)
A1	0	5.67	50.39	158.87	70.98
A2	12	5.57	59.30	163.20	71.47
B1	12	11.28	60.50	159.14	62.74
B2	12	11.36	53.93	190.70	73.45
B3	12	11.64	56.86	161.38	84.62
C1	0	7.78	66.64	2.82	219.85
C2	0	4.53	66.15	8.48	274.08
C3	0	10.12	65.10	11.95	338.62

4.2.1. The Results of Track A

Figure 8a,b presents the measured reverberation intensity and model outcomes for the first element of the receiving array at positions A1 and A2, respectively. Both of the figures demonstrate that the model calculations accord with the experimental results. The reverberation signals appear within 4.1 s to 15 s, and the intensity gradually decreases with time. According to the eigenrays and the corresponding arrival times presented in Figures A1 and A2 in Appendix B, the first peak in Figure 8a corresponds to the direct (D) ray and the surface reflection (SR) ray, and the second peak corresponds to the primary bottom reflection rays. In Figure 8b, three peaks correspond to D and SR, primary and secondary bottom reflection rays. Additionally, the primary bottom reflection rays consist of four types, namely, the bottom reflection (BR) ray, the bottom-surface reflection (BSR) ray, the surface-bottom reflection (SBR) ray and the surface-bottom-surface reflection (SBSR) ray.

Table 3 presents the value of the exit grazing angle at the source. At positions A1 and A2, although minor variation exists in the receiving range (r_{SR}) and the receiving depth (z_r), the arrival structures of the received signal are similar in both figures. However, when the transmitting beam angle is adjusted from 0° to 12°, the amplitudes of the multipath components change significantly. In Figure 8a, the exit grazing angles of D and SR are close to 0°, that is, the two rays lie on the main lobe of the transmitted beam, where the amplitudes are the highest. Whereas, the exit grazing angles of the four bottom reflection rays are far away from the main lobe, thus, their amplitudes are not as strong.

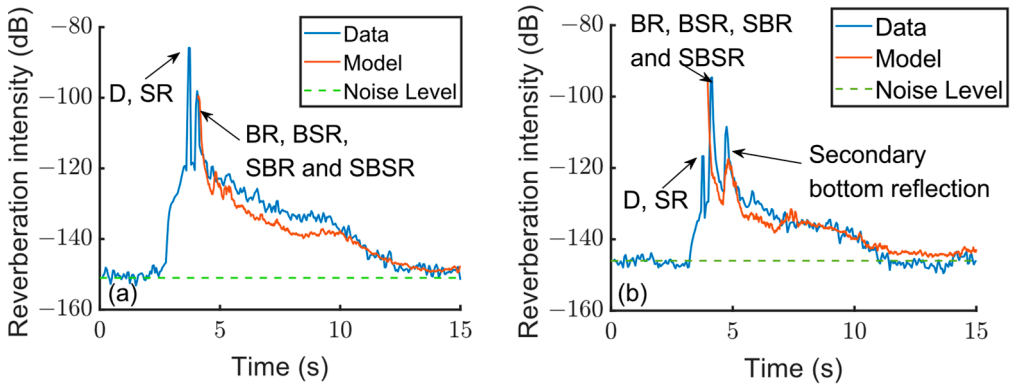


Figure 8. Comparison of the measured reverberation intensity with the model result for the first element of the receiving array at positions A1 and A2. (**a**) Position A1. (**b**) Position A2.

Table 3. The exit grazing angle of the eigenrays at the source.

Position	The Exit Grazing Angle at the Source					
	D	**SR**	**BR**	**BSR**	**SBR**	**SBSR**
A1	−1.85°	−2.02°	14.87°	16.46°	−16.51°	−17.92°
A2	−1.83°	−2.10°	15.12°	16.91°	−16.77°	−18.35°

The transmitting beam angle is 12° in Figure 8b. In this scene, the exit grazing angles of BR and BSR lie within the main lobe, while the exit grazing angles of D and SR are away from the beam angle. Consequently, the amplitudes of BR and BSR are higher than those of D and SR. Additionally, the amplitudes of the secondary bottom reflection increase. Only the signals scattered from the seafloor are taken into account; therefore, the model is incapable of calculating the direct and sea surface reflections between the source and the receiver. Due to the difference between the recorded parameters (such as source depth and receiving range) and the actual values in the experiment, as well as the relief of the seafloor, the intensity curve output by the model presents a certain deviation from the measured data.

Figure 9 shows the variations in reverberation intensity over time in beam domain on the Track A. Here, Figure 9a,c presents the experimental results at positions A1 and A2, and Figure 9b,d shows the corresponding simulations, respectively. The simulations present similar spatial-temporal structures and the intensity distribution of the bottom reverberation to the experimental results. The overall structures exhibit a "| < >" shape in the beam-time domain, corresponding to vertical, convex, and concave stripes. Moreover, the reverberation intensity gradually decreases with time at each beam output.

Figure 9a shows that peaks appear at 3.84 s and 4.1 s at a receiving beam angle of −6.8 degrees. Here, the first peak corresponds to D and SR, and the second peak corresponds to the four paths of the primary bottom reflection. In the mirror reflection direction, the propagation time of the aforementioned eigenrays reaching the receiver is earlier than in other directions. When the receiving beam angle varies, the amplitudes of the eigenrays entering from the side lobes remain high at these specific times. Therefore, the amplitude distribution of these eigenrays across the whole receiving beam angles constitutes the vertical stripes within the spatial-temporal structures of the bottom reverberation.

The convex and concave stripes are formed by the contribution of the scattered eigenrays from the seafloor grids. The convex stripe emerges after the primary bottom reflection, ranging from 4.1 s to 7.5 s, and the extent of the stripe gradually expands over time in the beam domain. Subsequently, the concave stripe emerges within the period from 7.5 s to 10 s.

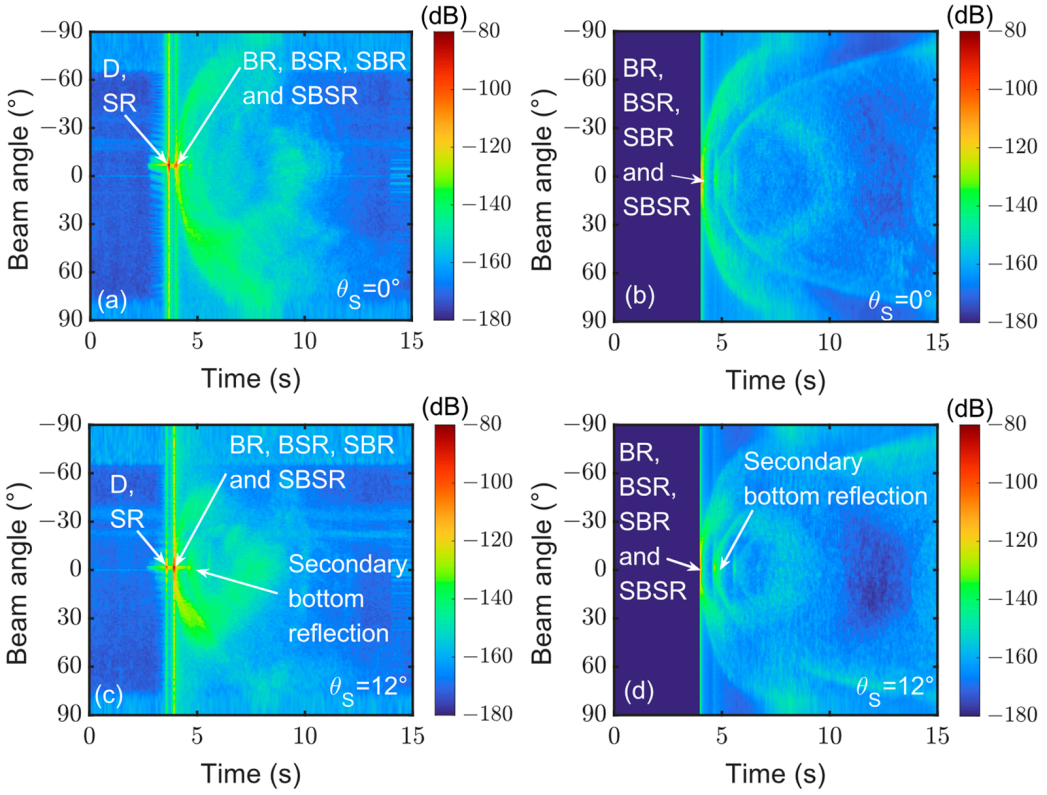


Figure 9. Comparison of experimental results and model outputs in the beam domain at positions A1 and A2. (**a**) Experimental results at position A1. (**b**) Model outputs at position A1. (**c**) Experimental results at position A2. (**d**) Model outputs at position A2.

According to the results illustrated in Figure A4 in Appendix C, which is the spatial distribution of scatterers that contribute to the reverberation at position A1, it is evident that scatterers contributing to the reverberation at a specific time are not completely located on the same ellipse, but are dispersed across multiple ellipses. At a specific time, t = 4 s, the bottom reverberation is mainly from scattered signals of seabed grids in the mirror reflection direction. As time progresses, scattered signals from multiple directions reach the receiving array, resulting in the appearance of the convex stripe in bottom reverberation. As transmission loss increases with distance, the intensity and extent of this stripe are lower than the vertical stripe. At time t = 8 s, an arc is formed by the grids with higher amplitudes in the region between the source and the receiver. These grids are distributed near the mirror reflection direction, corresponding to the span of the concave stripes. Furthermore, the uplifted terrain to the northeast of the source results in relatively strong scattering. Consequently, the reverberation intensity is markedly higher at positive received beam angles compared to negative angles.

The spatial-temporal structures depicted in Figure 9c are analogous to those in Figure 9a. Since the transmitting beam angle is directed toward the sea floor, the extent of certain reflection areas is reduced. Consequently, the convex and concave stripes extend over a span of angles from −45 to 45 degrees, narrower than the range from −85 to 85 degrees in Figure 9a. Similarly, the reverberation intensity at positive angles is significantly higher than at negative angles. As illustrated in Figure 7, the topographic relief exists northeast of the source, and there is likely relatively strong scattering generated in this area.

4.2.2. The Results of Track B and Track C

This section presents the experimental results and simulations for the other two tracks. Figures 10 and 11 illustrate the experimental results and the model outputs for Track B and C, respectively. Similar to the illustration for Track A, the model outputs accord with the experimental results for these two tracks, demonstrating comparable spatial-temporal structures for the bottom reverberation.

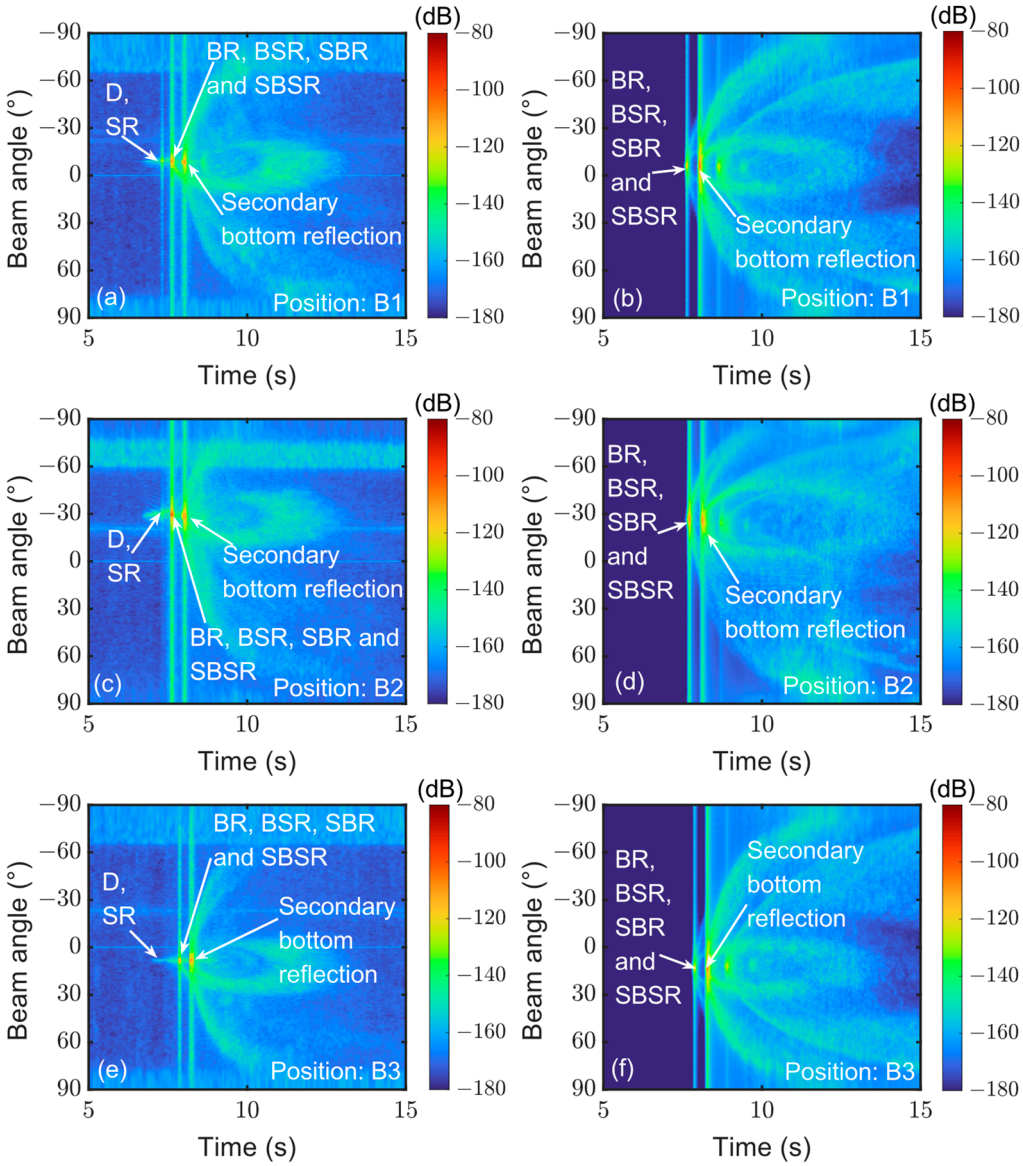


Figure 10. Comparison of experimental results and model outputs in the beam domain at positions B1, B2, and B3. (**a**) Experimental results at position B1. (**b**) Model outputs at position B1. (**c**) Experimental results at position B2. (**d**) Model outputs at position B2. (**e**) Experimental results at position B3. (**f**) Model outputs at position B3.

The receiving range r_{SR} and the heading angle γ at three positions of Track B are proximate, and the spatial-temporal structures presented in Figure 10a,c,e are similar. Meanwhile, the corresponding simulations at the positions are comparable. The receiving vessel moves from position B1 to B3, and the stripe structures shift from negative to positive angles.

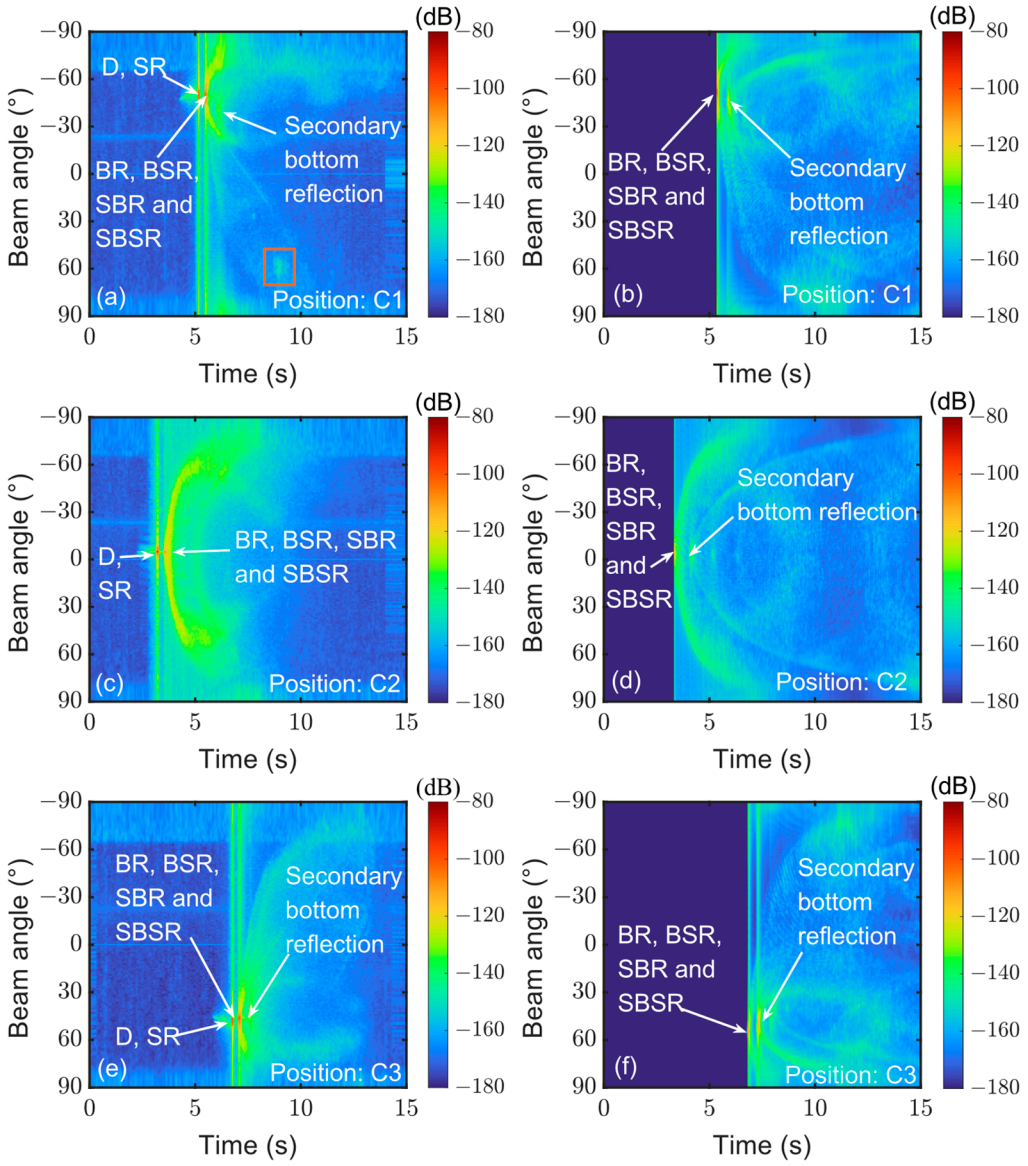


Figure 11. Comparison of experimental results and model outputs in the beam domain at positions C1, C2, and C3. (**a**) Experimental results at position C1. (**b**) Model outputs at position C1. (**c**) Experimental results at position C2. (**d**) Model outputs at position C2. (**e**) Experimental results at position C3. (**f**) Model outputs at position C3.

Two vertical stripes exist within the spatial-temporal structures after D and SR, corresponding to the primary and secondary bottom reflection, respectively. Certain disparities exist between the stripe structures in Track B and Track A. Specifically, as the main lobe of the transmitting beam is directed toward the seafloor, the amplitudes of the secondary bottom reflection increase.

The eigenrays, amplitudes, and arrival times presented in Figure A3 in Appendix B show that, although transmitting beam angles, θ_S, are the same for positions A2 and B1, exit grazing angles of eigenrays at the source are different. At position A2, the exit grazing angle of the secondary bottom reflection lies within the trough between the first and second sidelobes of the transmitting beam, leading to a low amplitude. In contrast, the exit grazing angle of the secondary bottom reflection is nearly aligned with the main lobe of the transmitting beam angle, resulting in a significantly higher amplitude relative to that at position A2. Furthermore, the concave stripe changes into an elliptical stripe following the convex stripe, and this stripe is concentrated in the proximity of the mirror reflection

direction. Based on the simulation illustrated in Figure A5 of Appendix C, it is observed that the scatterers contributing to the bottom reverberation depicted in Figure A5b–d are predominantly distributed along multiple ellipses in the area between the source and the receiver. The spatial distribution of scatterers in these three figures exhibits consistency across different time, and the scattered signals at these grids are the primary contributors to the formation of elliptical stripes.

Regarding the Track C results depicted in Figure 11, the positions ranging from C1 to C3 exhibit significant variations, and the stripe structures at the three positions present distinctions. At position C2, the source is in the broadside beam of the horizontal array. The stripe structures in Figure 11c,d are comparable to those at position A1, with a symmetrical distribution around a receiving beam angle of 0°.

Comparing Figure 11a,e, shows that the two stripes are similar, but their positions are situated at different angles. At positions C1 and C3, the incidence angles of the source are proximate to the negative and positive end-fire directions of the receiving array, respectively. The convex stripe and the subsequent elliptical stripe cover a narrow region of angles, and the region is concentrated near the mirror reflection direction.

At position C1, the source is situated within the negative receiving beam angle, in proximity to the negative end-fire direction of the receiving array. The region of scatterers significantly contributing to reverberation primarily encompasses the flat terrain in the mirror reflection direction, as well as the uplifted terrains to the northeast of the source and the receiver. Since position C1 is close to the boundary on the southwest of the experimental area, accordingly, the intensity of the upper half of the elliptical stripe is higher than that of the lower half. For position C3, situated in the southeast of the experimental area, the source is positioned at a positive receiving beam angle, proximate to the end-fire direction at the tail of the receiving array. The region of scatterers contributing to reverberation primarily encompasses the area in the mirror reflection direction, the uplifted terrain in the northeast of the source, and the uplifted terrain to the west of the receiver. Consequently, the intensity of the upper and lower halves in the elliptical stripe is contrary to that in position C1. Meanwhile, the simulations in Figure 11b,d generate results consistent with the above-mentioned phenomena.

In addition, significant scattering echoes exist within the rectangle in Figure 11a, corresponding to a receiving beam angle of 60° and a time ranging from 8.8 s to 9.3 s. This phenomenon was not discovered in other experimental results or simulations. The experimental records show that a fish shoal was near position C1, and we hypothesize that the echoes resulted from the fish scattering.

4.3. Interpretation of Stripes Observed in the Beam Output

To determine which eigenrays primarily constitute the stripe structures, the proposed model is employed in this section to simulate bottom reverberation under diverse combinations by setting the types of incident and scattered eigenrays.

Figure 12 depicts the types of incident eigenrays from the source to the seafloor and scattered eigenrays from the seafloor to the receiver. Based on the number of eigenrays contacting the seafloor, the types of incident and scattered eigenrays are labeled with numbers. Specifically, the number 0 is employed to mark D and SR, the number 1 is utilized to mark BSR and the SBSR, and so forth. Since the amplitude of secondary and multiple reflection rays is minor in the two planes, four combinations of incident and scattered eigenrays are accounted for in Figure 12. The combinations in Figure 12a–d are as follows: as: (a) D/SR-D/SR (type “00”); (b) D/SR-BSR/SBSR (type “01”); (c) BSR/SBSR-D/SR (type “10”); and (d) BSR/SBSR-BSR/SBSR (type “11”). At a specific scatterer in the mirror reflection direction, $\alpha_{\text{inc}} = \alpha_{\text{scatt}}$, at which point the combination constitutes

eigenrays between the source and the receiver, corresponding to primary and secondary bottom reflections.

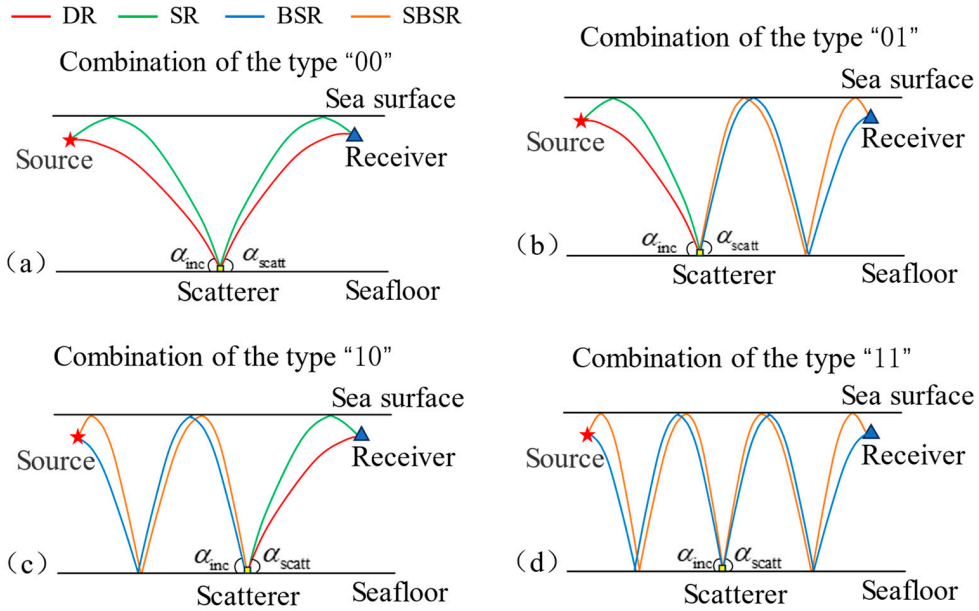


Figure 12. Types of eigenrays from the source to the seafloor scatterer and then to the receiver. (**a**) D/SR-D/SR (type "00"). (**b**) D/SR-BSR/SBSR (type "01"). (**c**) BSR/SBSR-D/SR (type "10"). (**d**) BSR/SBSR-BSR/SBSR (type "11").

Figures 13–15 exhibit reverberation simulations for the four types of combinations at positions A1, B1, and C1, respectively. In the simulation of the three positions, the transmitting beam angles are consistent with those specified in Table 2, which are 0 degrees, 12 degrees, and 0 degrees, respectively. Compared with the outcomes presented in Section 4.2, the four types of combinations exert a significant influence on the spatial-temporal structures of bottom reverberations. The simulations presented in Figures 13–15 demonstrate consistent regularity.

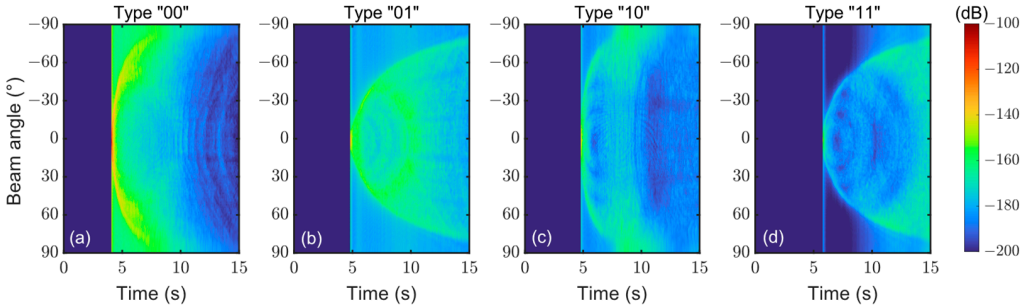


Figure 13. Reverberation simulation outcomes for the combination of the four types at position A1. (**a**) D/SR-D/SR. (**b**) D/SR-BSR/SBSR. (**c**) BSR/SBSR-D/SR. (**d**) BSR/SBSR-BSR/SBSR.

Figures 13–15 show that the "00" type significantly impacts the vertical and convex stripes within the reverberation structures. This type corresponds to the D and SR rays from the source to the seafloor scatterer, as well as those from the seafloor scatterer to the receiver. Similarly, the "01" type predominantly influences the concave or elliptical stripes. Moreover, the "10" and the "11" types exert influences on the above two parts of the stripe structures, respectively. However, the amplitudes of the eigenrays in these two types are lower than those of the initial two types. Figure 14 shows that as the transmitting beam angle is adjusted to 12 degrees, the amplitude of BSR in the incident plane increases,

and the intensity in Figure 14c is higher than in Figure 14a. Accordingly, the vertical and convex stripes are mainly influenced by the "10" type. Nevertheless, similar to the outcomes in Figures 13b and 15b, the "01" type still exerts a predominant influence on the elliptical stripe.

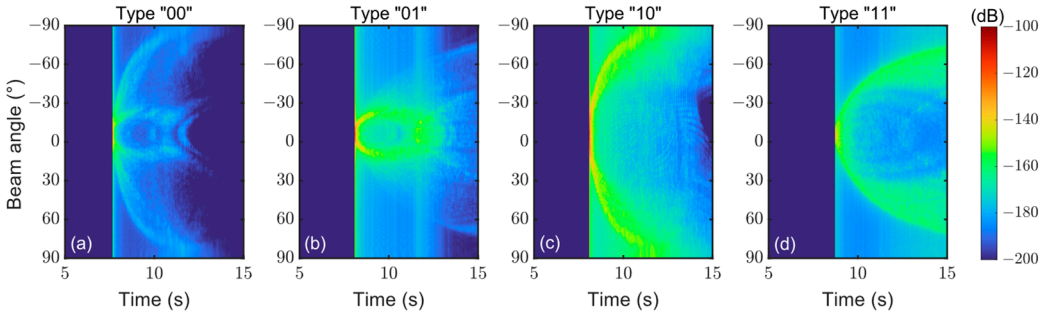


Figure 14. Reverberation simulation outcomes for the combination of the four types at position B1. (**a**) D/SR-D/SR. (**b**) D/SR-BSR/SBSR. (**c**) BSR/SBSR-D/SR. (**d**) BSR/SBSR-BSR/SBSR.

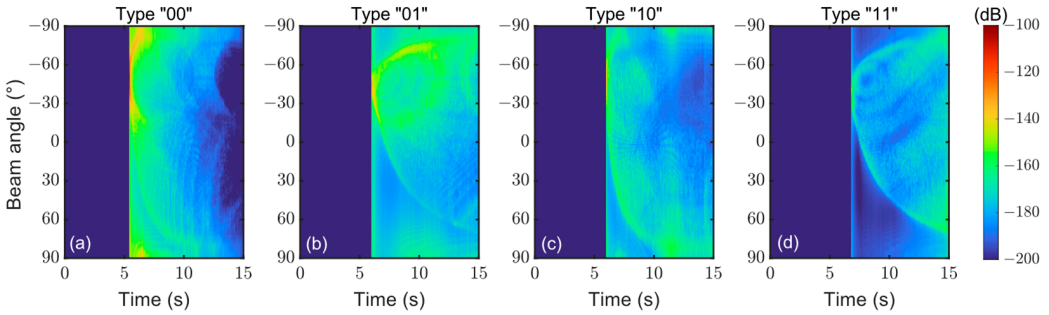


Figure 15. Reverberation simulation outcomes for the combination of the four types at position C1. (**a**) D/SR-D/SR. (**b**) D/SR-BSR/SBSR. (**c**) BSR/SBSR-D/SR. (**d**) BSR/SBSR-BSR/SBSR.

Additionally, the morphological characteristics of the reverberation for the "00" type are analogous to those of the "10" type, while the morphologies of the reverberation corresponding to the "01" type are comparable to those of the "11" type. According to the equation in Section 2 ($\sin\theta'_{i,n} = \sin\theta_i \cos\beta_{Rn}$), the arrival angle $\theta'_{i,n}$ of the nth scattered eigenray is determined by the variables θ_i and β_{Rn}. The former variable corresponds to the angle between the scattering plane and the normal direction of the receiving array, and the latter corresponds to the grazing angle of the scattered eigenray at the receiver. This suggests that, for various combinations of incident and scattered eigenrays, the D and SR rays within the scattered eigenrays primarily affect the convex stripe, while the BSR and the SBSR rays have a more substantial impact on the concave or elliptical stripe.

This comparison of the tracks demonstrates the effectiveness of the model in simulating bottom reverberation. The experimental results and simulations indicate that the vertical stripes within the spatial-temporal structures are formed by the bottom reflected rays in the mirror reflection direction. Furthermore, the curved and elliptical stripes result from the combined effect of the incident and scattered eigenrays from the seafloor scatterers in different areas.

5. Summary and Conclusions

In this paper, a bistatic bottom reverberation model is proposed to model and analyze the spatial-temporal structures of ocean bottom reverberation signals received by a towed horizontal array. Based on ray theory and the SSA scattering model, the model simulates signals in the beams of the array.

Unlike the empirical function scattering model [15,34], the SSA model is applicable to the full span of grazing angles, as the former is merely applicable to small grazing angles. The beam pattern considers the impact of each scatterer on the reverberation intensity, which is more feasible and applicable than dividing the seafloor regions to simulate reverberation at specific receiving beam angles.

The comparison between the simulation and experimental results indicates that the model outputs reproduce the stripe structures of reverberation in the experiment. The stripe structures encompass vertical, curved, and elliptical stripes. Moreover, the bottom reverberation under various combinations is simulated by setting the types of incident and scattered eigenrays. The analysis indicates that the vertical stripes are generated by the bottom reflection eigenrays in the mirror reflection direction. Meanwhile, the convex and concave stripes, as well as the elliptical stripes, are formed through a combination of incident and scattered eigenrays. The convex stripes are mainly influenced by the D and SR rays within the scattered eigenrays, while the concave and elliptical ones are primarily impacted by the BSR and SBSR rays.

The established model has some limitations. Firstly, an $N \times 2D$ ray model is employed to address the varying seabed topography. For environments with abrupt topographic variations such as seamounts, the model does not account for the effects of horizontal refraction [39]. Such changes will affect the eigenray structure, and result in model outputs being inconsistent with the true results. Secondly, the seabed substrate in the actual environment is multi-layered and complex, and the parameters significantly affect the reverberation intensity output of the model. Due to utilizing a single-layer seabed in the model and unknown parameters, certain disparities exist between the model output and the experimental results. Correspondingly, some stripes cannot be observed in the experiment. Considering these problems, we propose the following solutions: For the first case, the three-dimensional sound field model can be employed to address complex topography, providing more accurate calculations such as the propagation delays and amplitudes of the eigenrays. In the second case, accurate environmental parameters are obtained and a multi-layer seabed model can be employed. The extensive prior information enhances the model outputs, ensuring consistency with the experimental results.

There are potential enhancements for future research. For example, considering variations in seabed topography and prevalent oceanic phenomena, it is valuable to improve and extend the model to accurately predict the intensity and spatial-temporal structures of reverberation within complex environments. Furthermore, the parameters of the seabed substrate can be retrieved utilizing the model. In addition, by analyzing the stripe structures presented in both the model output and the measured data, it becomes possible to distinguish the seabed features or potential targets.

Author Contributions: Conceptualization, Z.S. and J.Z.; methodology, Z.S. and J.Z.; software, Z.S.; validation, Z.S., J.Z. and C.S.; formal analysis, Z.S., J.Z. and C.S.; investigation, Z.S.; resources, J.Z. and C.S.; data curation, Z.S.; writing—original draft preparation, Z.S.; writing—review and editing, J.Z. and C.S.; supervision, J.Z. and C.S.; project administration, J.Z. and C.S.; funding acquisition, J.Z. and C.S. All authors have read and agreed to the published version of the manuscript.

Funding: This work was supported by the National Key R&D Program of China (2016YFC1400104).

Data Availability Statement: The data presented in this study are available from the corresponding author on request.

Acknowledgments: The sea experiment was organized and carried out by Zhejiang University. We sincerely thank all individuals who participated in the acoustic experiment in the South China Sea in August 2020. Their diligent efforts provided reliable experimental data.

Conflicts of Interest: The authors declare no conflicts of interest.

Appendix A

The representation of $R_{ww}(\alpha_{\mathrm{inc},m}, \alpha_{\mathrm{scatt},n}, \varphi_i)$ for Equation (4) in Section 2 varies depending on the type of seafloor substrate utilized. In this study, a standard fluid substrate was employed for the seafloor. The formulas are as follows:

$$R_{ww}(\alpha_{\mathrm{inc},m}, \alpha_{\mathrm{scatt},n}, \varphi_i) = \frac{1}{2}[1 + V_{ww}(\alpha_{\mathrm{inc},m})][1 + V_{ww}(\alpha_{\mathrm{scatt},n})]O_{wp} \tag{A1}$$

$$O_{wp} = \left(1 - \frac{1}{a_\rho}\right)\left(\cos\alpha_{\mathrm{inc},m}\cos\alpha_{\mathrm{scatt},n}\cos\varphi_i - o_{wp}\right) - 1 + \frac{1}{a_{wp}^2 a_\rho} \tag{A2}$$

$$o_{wp} = \frac{\sqrt{1 - a_{wp}^2\cos^2\alpha_{\mathrm{inc},m}}\sqrt{1 - a_{wp}^2\cos^2\alpha_{\mathrm{scatt},n}}}{a_{wp}^2 a_\rho} \tag{A3}$$

$$V_{ww} = \frac{Z_{wp} - 1}{Z_{wp} + 1} \tag{A4}$$

$$Z_{wp} = \frac{a_{wp}a_\rho\sin\alpha}{\sqrt{1 - a_{wp}^2\cos^2\alpha}} \tag{A5}$$

where a_ρ represents the ratio of the density at the bottom to that in the water, and a_{wp} represents the ratio of the speed at the bottom to that in the water. The variable α denotes either $\alpha_{\mathrm{inc},m}$ or $\alpha_{\mathrm{scatt},n}$ depending on the V_{ww} in Equation (A1).

Appendix B

Based on the Bellhop model [38], we simulated the structures, arrival times, and exit grazing angle of eigenrays at the source.

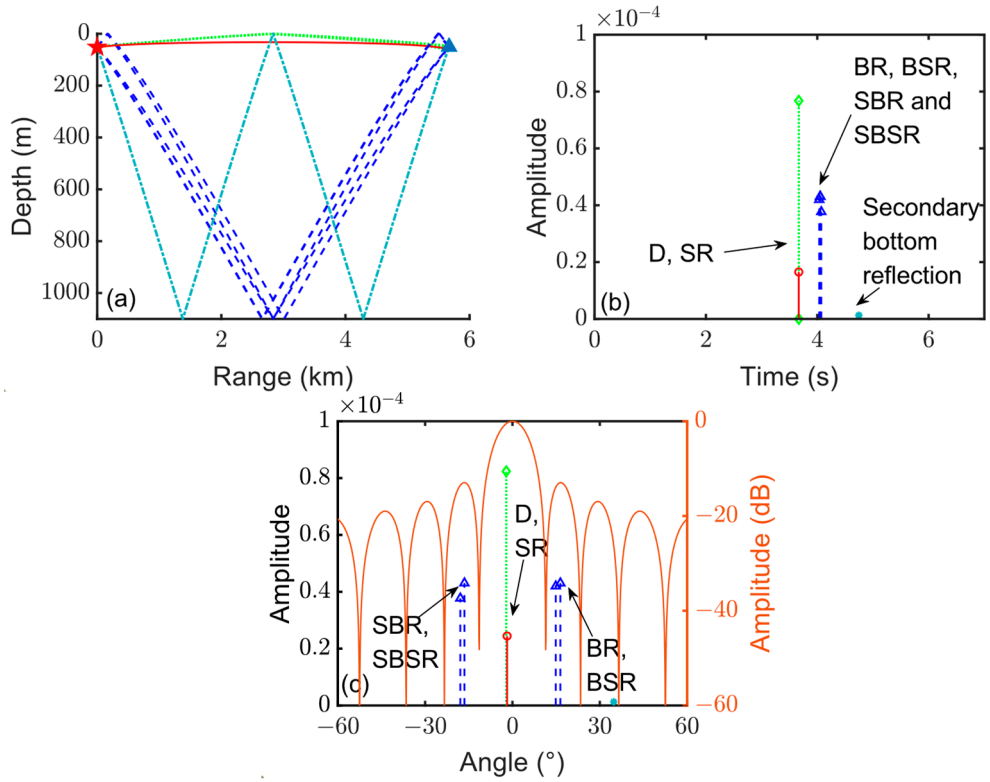


Figure A1. The eigenrays, arrival times, and exit grazing angle at the source at position A1. (**a**) Eigenrays. (**b**) Arrival times. (**c**) Exit grazing angles of eigenrays and the beam pattern of the transmitting array.

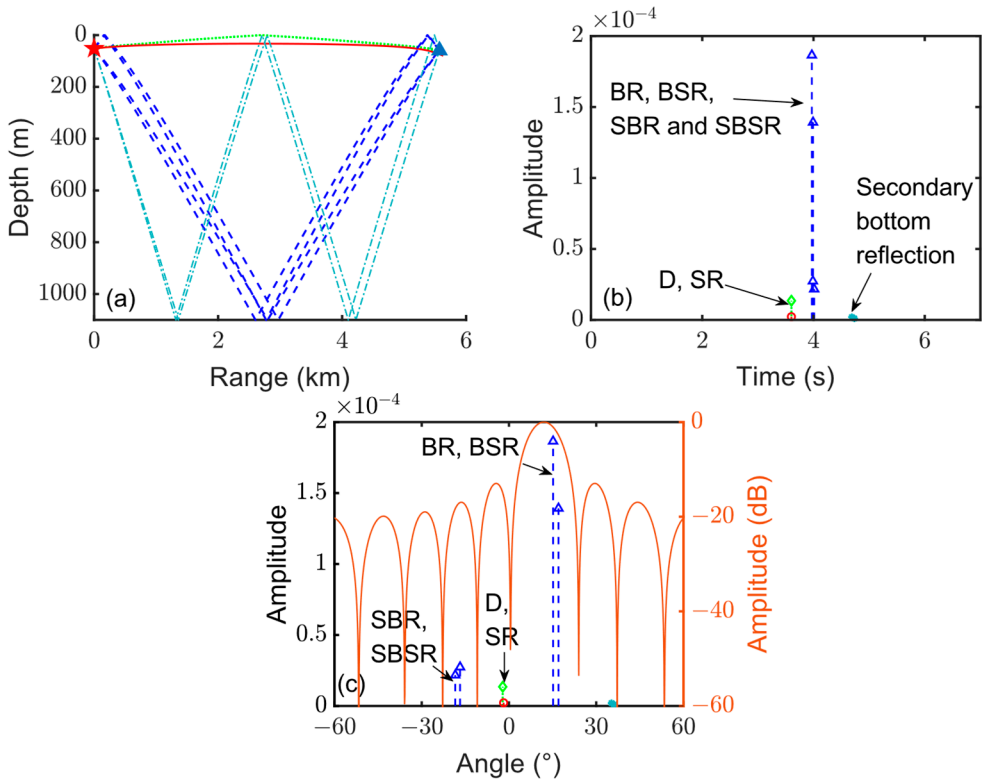


Figure A2. The eigenrays, arrival times, and exit grazing angle at the source at position A2. (**a**) Eigenrays. (**b**) Arrival times. (**c**) Exit grazing angles of eigenrays and the beam pattern of the transmitting array.

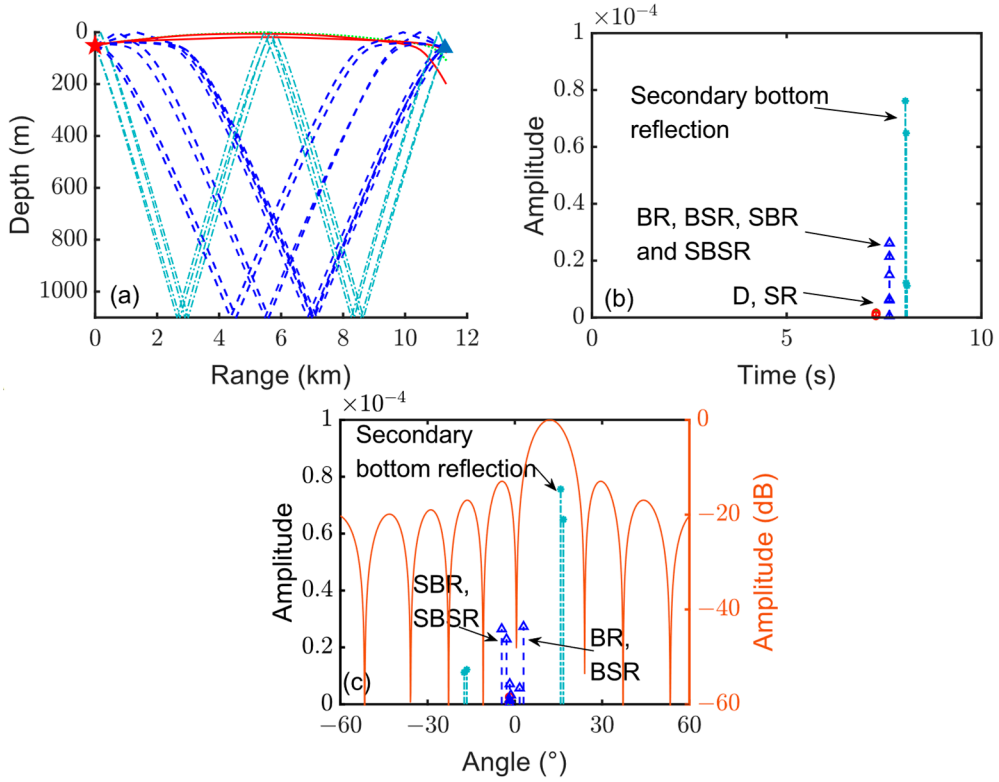


Figure A3. The eigenrays, arrival times, and exit grazing angle at the source at position B1. (**a**) Eigenrays. (**b**) Arrival times. (**c**) Exit grazing angles of eigenrays and the beam pattern of the transmitting array.

Appendix C

Taking positions A1 and B1 as examples, we computed the positions of the scatterers contributing to bottom reverberation and corresponding amplitudes on the grid. The results are shown in Figures A4 and A5, respectively.

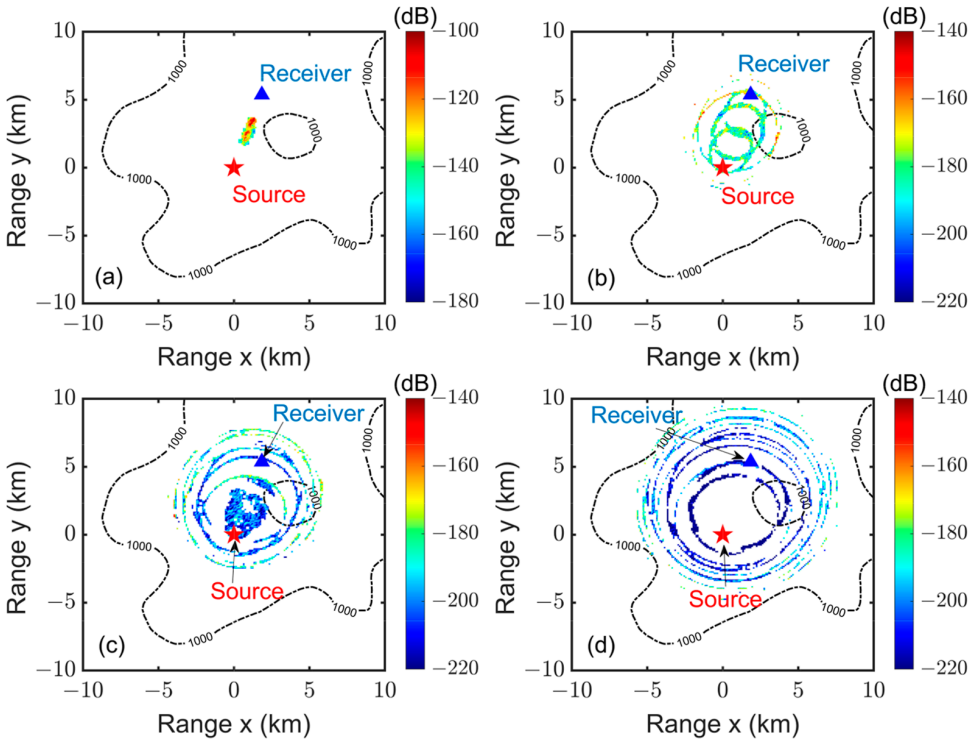


Figure A4. The positions of the scatterers contributing to the reverberation vary over time at position A1. (**a**) t = 4 s. (**b**) t = 6 s. (**c**). t = 8 s. (**d**) t = 10 s.

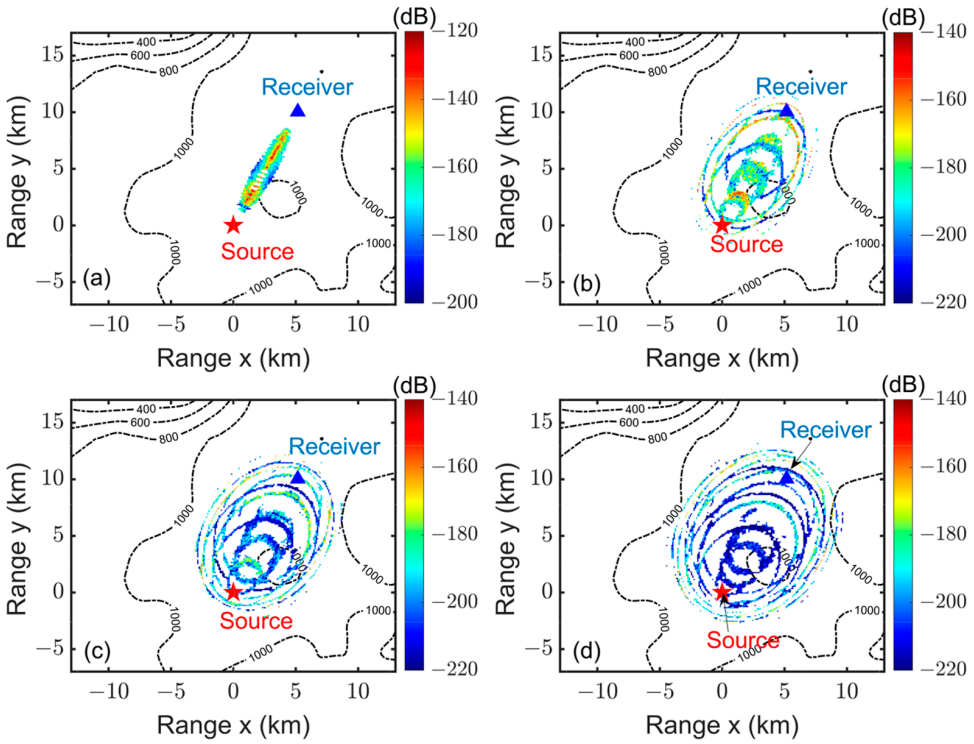


Figure A5. The positions of the scatterers contributing to the reverberation vary over time at position B1. (**a**) t = 7.65 s. (**b**) t = 9.5 s. (**c**). t = 10.5 s. (**d**) t = 11.5 s.

References

1. Zheng, G.; Guo, X.; Zhu, F.; Wang, F.; Bai, L. Analysis of bottom reverberation intensity under beam-controlled emission conditions in deep water. *Arch. Acoust.* **2024**, *49*, 221–231. [CrossRef]
2. Wang, L.; Huang, Y.; Guo, L.; Ren, C. Acoustic scattering modeling and sound field characteristics of rough seafloor in shallow sea. *Acta Phys. Sin.* **2024**, *73*, 034301. [CrossRef]
3. Xu, L.; Yang, K.; Yang, Q. Geoacoustic Inversion Using Physical–Statistical Bottom Reverberation Model in the Deep Ocean. *Acoust. Aust.* **2019**, *47*, 261–269. [CrossRef]
4. Yang, K.; Xu, L.; Yang, Q.; Li, G. Two-Step Inversion of Geoacoustic Parameters with Bottom Reverberation and Transmission Loss in the Deep Ocean. *Acoust. Aust.* **2018**, *46*, 131–142. [CrossRef]
5. Guo, Y.; Duan, R.; Zhang, H.; Yang, K.; Liu, T.; Gong, G. Modeling and interpretation of bistatic bottom reverberation in deep water near seamounts. *J. Acoust. Soc. Am.* **2023**, *154*, 3173–3187. [CrossRef]
6. Ratilal, P.; Lai, Y.; Symonds, D.T.; Ruhlmann, L.A.; Preston, J.R.; Scheer, E.K.; Garr, M.T.; Holland, C.W.; Goff, J.A.; Makris, N.C. Long Range Acoustic Imaging of the Continental Shelf Environment: The Acoustic Clutter Reconnaissance Experiment 2001. *J. Acoust. Soc. Am.* **2005**, *117*, 1977–1998. [CrossRef]
7. Zheng, Y.; Ping, X.; Li, L.; Wang, D. Maximum Likelihood Deconvolution of Beamforming Images with Signal-Dependent Speckle Fluctuations. *Remote Sens.* **2024**, *16*, 1506. [CrossRef]
8. Tang, D.; Jackson, D. Application of small-roughness perturbation theory to reverberation in range-dependent waveguides. *J. Acoust. Soc. Am.* **2012**, *131*, 4428–4441. [CrossRef]
9. Ivakin, A. A full-field perturbation approach to scattering and reverberation in range-dependent environments with rough interfaces. *J. Acoust. Soc. Am.* **2016**, *140*, 657–665. [CrossRef]
10. Tang, D.; Jackson, D. A time-domain model for seafloor scattering. *J. Acoust. Soc. Am.* **2017**, *142*, 2968–2978. [CrossRef]
11. Wu, J.; Gao, T.; Shang, E. Reverberation Intensity Decaying in Range-Dependent Waveguide. *J. Theor. Comput. Acoust.* **2019**, *27*, 1950007. [CrossRef]
12. Bucker, H.; Morris, H. Normal-mode reverberation in channels or ducts. *J. Acoust. Soc. Am.* **1968**, *44*, 827–828. [CrossRef]
13. Ellis, D.D. A shallow-water normal-mode reverberation model. *J. Acoust. Soc. Am.* **1995**, *97*, 2804–2814. [CrossRef]
14. Li, N.; Zhang, M.; Gao, B. Horizontal Correlation of Long-Range Bottom Reverberation in Shallow Sloping Seabed. *J. Mar. Sci. Eng.* **2021**, *9*, 414. [CrossRef]
15. Wang, L.; Qin, J.; Fu, D.; Li, Z.; Liu, J.; Weng, J. Bottom reverberation for large receiving depth in deep water. *Acta Phys. Sin.* **2019**, *68*, 134303. [CrossRef]
16. Guo, R.; Lei, L.; Sheng, Z.; Song, P. A three-dimensional bistatic reverberation model of underwater explosion by interface scattering at variable sound speeds. *J. Low Freq. Noise Vib. Act. Control* **2019**, *38*, 427–440. [CrossRef]
17. Bouchage, G.; Zakharia, M.; LePage, K.D. A Bottom Reverberation Model Based on the Coupling Between Parabolic Equation and Scattering Strengths. *Acta Acust. United Acust.* **2012**, *98*, 216–222. [CrossRef]
18. Lingevitch, J.F.; Fromm, D.M.; LePage, K.D. Parabolic equation technique for reverberation modeling. *J. Acoust. Soc. Am.* **2007**, *122*, 3074. [CrossRef]
19. Makris, N.C.; Avelino, L.Z.; Menis, R. Deterministic Reverberation from Ocean Ridges. *J. Acoust. Soc. Am.* **1995**, *97*, 3547–3574. [CrossRef]
20. Makris, N.C.; Chia, C.S.; Fialkowski, L.T. The Bi-Azimuthal Scattering Distribution of an Abyssal Hill. *J. Acoust. Soc. Am.* **1999**, *106*, 2491–2512. [CrossRef]
21. Chia, C.S.; Makris, N.C.; Fialkowski, L.T. A Comparison of Bistatic Scattering from Two Geologically Distinct Abyssal Hills. *J. Acoust. Soc. Am.* **2000**, *108*, 2053–2070. [CrossRef] [PubMed]
22. Preston, J.R.; Ellis, D.D. Extracting Bottom Information from Towed-Array Reverberation Data: Part I: Measurement Methodology. *J. Mar. Syst.* **2009**, *78*, S359–S371. [CrossRef]
23. Ellis, D.D.; Preston, J.R. Extracting Bottom Information from Towed-Array Reverberation Data. Part II: Extraction Procedure and Modelling Methodology. *J. Mar. Syst.* **2009**, *78*, S372–S381. [CrossRef]
24. Jagannathan, S.; Küsel, E.T.; Ratilal, P.; Makris, N.C. Scattering from extended targets in range-dependent fluctuating ocean-waveguides with clutter from theory and experiments. *J. Acoust. Soc. Am.* **2012**, *132*, 680–693. [CrossRef] [PubMed]
25. Galinde, A.; Donabed, N.; Andrews, M.; Lee, S.; Makris, N.C.; Ratilal, P. Range-dependent waveguide scattering model calibrated for bottom reverberation in a continental shelf environment. *J. Acoust. Soc. Am.* **2008**, *123*, 1270–1281. [CrossRef]
26. Ellis, D.D.; Yang, J.; Preston, J.R.; Pecknold, S. A Normal Mode Reverberation and Target Echo Model to Interpret Towed Array Data in the Target and Reverberation Experiments. *IEEE J. Ocean. Eng.* **2017**, *42*, 344–361. [CrossRef]
27. Yang, J.; Tang, D.; Hefner, B.T.; Williams, K.L.; Preston, J.R. Overview of Midfrequency Reverberation Data Acquired During the Target and Reverberation Experiment 2013. *IEEE J. Ocean. Eng.* **2018**, *43*, 563–585. [CrossRef]
28. Preston, J.R.; Ellis, D.D.; Gauss, R.C. Geoacoustic parameter extraction using reverberation data from the 2000 Boundary Characterization Experiment on the Malta Plateau. *IEEE J. Ocean. Eng.* **2005**, *30*, 709–732. [CrossRef]

29. Prior, M.K. A Scatterer Map for the Malta Plateau. *IEEE J. Ocean. Eng.* **2005**, *30*, 676–690. [CrossRef]
30. Preston, J.R.; Abraham, D.A. Statistical Analysis of Multistatic Echoes from a Shipwreck in the Malta Plateau. *IEEE J. Ocean. Eng.* **2015**, *40*, 643–656. [CrossRef]
31. Holland, C.W.; Preston, J.R.; Abraham, D.A. Long-range acoustic scattering from a shallow water mud-volcano cluster. *J. Acoust. Soc. Am.* **2007**, *122*, 1946–1958. [CrossRef] [PubMed]
32. Jung, Y.; Seong, W.; Lee, K.; Kim, S. A Depth-Bistatic Bottom Reverberation Model and Comparison with Data from an Active Triplet Towed Array Experiment. *Appl. Sci.* **2020**, *10*, 3080. [CrossRef]
33. Jung, Y.; Lee, K. Observation of the Relationship between Ocean Bathymetry and Acoustic Bearing-Time Record Patterns Acquired during a Reverberation Experiment in the Southwestern Continental Margin of the Ulleung Basin, Korea. *J. Mar. Sci. Eng.* **2021**, *9*, 1259. [CrossRef]
34. Ellis, D.D.; Crowe, D.V. Bistatic reverberation calculations using a three-dimensional scattering function. *J. Acoust. Soc. Am.* **1991**, *89*, 2207–2214. [CrossRef]
35. Zhou, C.; Mo, D.; Gao, B. Seamount Clutter Modeling for Long Range Seabed Reverberation in Deep Sea. *J. Phys. Conf. Ser.* **2023**, *2486*, 012099. [CrossRef]
36. Gragg, R.F.; Wurmser, D.; Gauss, R.C. Small-slope scattering from rough elastic ocean floors: General theory and computational algorithm. *J. Acoust. Soc. Am.* **2001**, *110*, 2878–2901. [CrossRef]
37. Neighbors, T.H.; Bradley, D. *Applied Underwater Acoustics (Leif Bjørnø)*, 1st ed.; Elsevier: Amsterdam, The Netherlands, 2017; Chapter 8, pp. 482–486.
38. The Bellhop Model Was Acquired from the Acoustic Toolbox, Version 2020_11_4. Available online: http://oalib.hlsresearch.com/AcousticsToolbox (accessed on 20 November 2024).
39. Li, S.; Li, Z.; Li, W.; Yu, Y. Three-Dimensional Sound Propagation in the South China Sea with the Presence of Seamount. *J. Mar. Sci. Eng.* **2021**, *9*, 1078. [CrossRef]

Disclaimer/Publisher's Note: The statements, opinions and data contained in all publications are solely those of the individual author(s) and contributor(s) and not of MDPI and/or the editor(s). MDPI and/or the editor(s) disclaim responsibility for any injury to people or property resulting from any ideas, methods, instructions or products referred to in the content.